Improved Statistical Efficiency of Simultaneous Multi-Slice fMRI by Reconstruction with Spatially Adaptive Temporal Smoothing

Mark Chiew[1], Karla L. Miller[1]

[1]Wellcome Centre for Integrative Neuroimaging, FMRIB, Nuffield Department of Clinical Neurosciences, University of Oxford

Corresponding Author:
Mark Chiew
FMRIB Centre
John Radcliffe Hospital
Oxford
OX3 9DU
Email: mark.chiew@ndcn.ox.ac.uk

Abstract

We introduce an approach to reconstruction of simultaneous multi-slice (SMS)-fMRI data that improves the statistical efficiency of general linear model (GLM) regression. The method incorporates regularization to adjust temporal smoothness in a spatially varying, encoding-dependent manner, reducing the g-factor noise amplification per temporal degree of freedom. This results in a net improvement in the statistical efficiency of a GLM analysis, where the efficiency gain is derived analytically as a function of the reconstruction parameters. Residual slice leakage and aliasing is limited when fMRI signal energy is dominated by low frequencies. Theoretical, simulated and experimental results demonstrate a marked improvement in GLM efficiency in the temporally regularized reconstructions compared to conventional SENSE and slice-GRAPPA reconstructions, particularly in central brain regions. Furthermore, experimental results confirm that residual slice leakage and aliasing errors are not noticeably increased compared to slice-GRAPPA reconstruction. This approach to temporally regularized image reconstruction in SMS-fMRI improves statistical power, and allows for explicit choice of reconstruction parameters by directly assessing their impact on GLM efficiency.

1. Introduction

Simultaneous multi-slice (SMS) imaging (Moeller et al., 2010) has become widely used for functional MRI (fMRI) data acquisition, particularly since the introduction of the controlled aliasing in parallel imaging (CAIPI) (Breuer et al., 2005) blipped EPI acquisition (Setsompop et al., 2012). The blipped CAIPI scheme significantly reduced noise amplification g-factor penalties associated with the SMS unaliasing by introducing a 3D k-space sampling pattern (Zhu et al., 2012) that manipulates aliasing locations to improve conditioning of the encoding matrix.

All SMS reconstruction methods rely on knowledge of the coil sensitivities (Pruessmann et al., 1999) or equivalently, the GRAPPA kernels (Griswold et al., 2002) for reconstruction. Broadly speaking, SMS reconstructions have employed either SENSE/GRAPPA (Blaimer et al., 2013, 2006; Koopmans, 2017; Moeller et al., 2014), Slice-GRAPPA (Cauley et al., 2014; Hoge et al., 2018; Setsompop et al., 2012, p. 2012), or conventional SENSE (Zahneisen et al., 2014) formulations. In addition to coil sensitivity information, SMS reconstruction using additional phase (Blaimer et al., 2013) or low-rank (coil x space) (Kim and Haldar, 2015; Park and Park, 2017) constraints have also been proposed. Some of these methods have been specifically designed to minimize reconstruction spatial bias (Cauley et al., 2014; Park and Park, 2017) that arises from inter-slice leakage artifacts.

All of the above methods operate in a time-independent manner, reconstructing images individually. In the context of functional MRI (fMRI), methods additionally exploiting temporal structure in the data have been demonstrated in compressed sensing approaches, (Chavarrías et al., 2015; Jung et al., 2007; Zong et al., 2014), or by minimizing image differences (Li et al., 2018). Alternatively, low-rank (space x time) methods have been proposed for use in fMRI based on the use of low-dimensionality representations in fMRI analysis methods (Chiew et al., 2016, 2015). While low-rank approaches do not impose any specific constraint on the representation of spatial or temporal information, more recent low-rank plus sparse methods have also been used to additionally exploit sparsity in the temporal Fourier domain (Aggarwal et al., 2017; Petrov et al., 2017; Singh et al., 2015; Weizman et al., 2017) which requires smoothness or periodicity in voxel time-courses.

Here, we introduce an improvement to SMS-EPI for fMRI by introducing time-varying sampling with a spatially adaptive temporally regularized reconstruction. Analytical expressions for reconstruction bias and variance are presented, as well as assessment of the relative statistical efficiencies of a general linear model (GLM) analysis as a function of the image reconstruction parameters. We exploit the low-frequency distribution of BOLD signals to ensure that the proposed reconstruction results in comparable or lower mean squared error than is produced by conventional SENSE or slice-GRAPPA unaliasing, while improving statistical power. This paper demonstrates the utility of this proposed reconstruction in

simulations and experiments, and provides a framework for principled analysis of temporal regularization factors in fMRI by directly calculating the impact of unaliasing reconstruction parameters on GLM analysis.

2. Theory

2.1 Linear Reconstruction

By considering SMS unaliasing to be a special case of a 3D under-sampling problem, a general SENSE-based framework can be used for reconstruction. The linear reconstruction problem we propose to solve is:

$$\min_x \|Ax - k\|_2^2 + \lambda \cdot R(x) \qquad [1]$$

where A is the linear encoding operator, which incorporates point-wise multiplication of coil sensitivities (assumed to be whitened) and the k-space sampling transform (which can be Cartesian or non-uniformly sampled). If the data vector x is formed by vertically concatenating the time-series images across time-points (into a $N_x N_y N_z N_t \times 1$ vector, with $N_{x,y,z}$ corresponding to spatial dimensions x, y and z, and N_t corresponding to the number of time-points), then A is a block-diagonal matrix where the block corresponding to time-point t is $\left[F_u^{(t)} S_1, \quad \cdots, \quad F_u^{(t)} S_c\right]^T$, with $F_u^{(t)}$ denoting the under-sampled Fourier transform at time t, and S_i is the sensitivity for the ith coil, for $1 \leq i \leq c$. In Eq. 1, k is the vectorized k-space data, R is the L2 penalty that enforces temporal smoothing, and λ is the parameter that controls the amount of smoothing and effective temporal resolution.

We choose R to be:

$$R(x) = \|\nabla x\|_2^2 = x\nabla'\nabla x \qquad [2]$$

where ∇ is the finite difference operator acting on the time domain (voxel-by-voxel), and ∇' denotes the adjoint of ∇. The L2 penalty allows the consequence of R to be interpreted like a linear smoothing operation, with the solution to Eq. 1 well known to be:

$$\hat{x} = (A'A + \lambda\nabla'\nabla)^{-1} A'k \qquad [3]$$

2.2 Reconstruction Bias and Variance

To characterize the estimator in Eq. 3, we consider the total mean squared reconstruction error as $MSE = bias^2 + variance$, where the bias term represents signal misallocation error (e.g. leakage or residual aliasing) and the variance term related to noise amplification (e.g. g-factor). We first reformulate Eq. 3 in terms of an equivalent, encoding dependent

smoothing operator, S_λ, that is applied following a conventional pseudoinverse reconstruction:

$$S_\lambda = (A'A + \lambda\nabla'\nabla)^{-1}(A'A) \qquad [4]$$

$$\hat{x} = S_\lambda (A'A)^{-1}A'k = S_\lambda A^\dagger k \qquad [5]$$

where $A^\dagger$ denotes the Moore-Penrose pseudoinverse of A. Using this formulation, it is apparent that S_λ is spatially adaptive in that it depends on $A'A$ (Fessler and Rogers, 1996), unlike conventional shift-invariant post-hoc kernel smoothing.

With $A^\dagger k = x$, the bias expected from this reconstruction can be described by:

$$E(\hat{x} - x) = S_\lambda A^\dagger k - x = [S_\lambda - I]x \qquad [6]$$

The g-factor at each time-point can be derived from the square root of the voxel-wise ratio of the variance of the estimator $\hat{x}$ and the variance of a fully sampled, unsmoothed reconstruction (see Eq. A9, Appendix A):

$$g_\lambda(m,t) = \sqrt{(S_\lambda (A'A)^{-1} S_\lambda{}')_{m,t}(A'A)_{m,t}} \qquad [7]$$

where here $M_{n,t}$ denotes the diagonal element of M corresponding to the nth voxel and t^{th} time-point, resulting in a g-factor for every voxel and time-point. The average g-factor for any voxel m is then given by the root-mean-square across time (Ramb et al., 2015):

$$\bar{g}_\lambda(m) = \sqrt{\frac{1}{N_t}\sum_t g_\lambda(m,t)} \qquad [8]$$

2.3 GLM Efficiency

The benefit of regularization, in the context of general linear model regression analysis, can be quantified by the efficiency of the estimator produced from the proposed reconstruction. Efficiency is inversely related to the variance of the estimated GLM regression coefficient, and an increase in efficiency results in increased statistical power.

A complete derivation of the relative efficiency between a regularized and un-regularized reconstruction can be found in Appendix B, following closely from Worsley and Friston (Worsley and Friston, 1995). Efficiency is a voxel-wise measure depending on g-factor, S_λ, and the task design matrix:

$$e_\lambda = \left(\frac{g_0}{g_\lambda}\right)^2 \left(\frac{DOF_\lambda}{DOF_0}\right)\left(\frac{(D'D)^{-1}}{(\widetilde{D}'\widetilde{D})^{-1}\widetilde{D}'S_\lambda S_\lambda{}'\widetilde{D}(\widetilde{D}'\widetilde{D})^{-1}}\right) \qquad [9]$$

where

$$DOF_\lambda = tr_m\left(\left(I - \widetilde{D}\left(\widetilde{D}'\widetilde{D}\right)^{-1}\widetilde{D}'\right)S_\lambda S_\lambda{}'\right) \qquad [10]$$

can be interpreted as an effective degrees of freedom (DOF) measure, where $\widetilde{D} = S_\lambda D$ is the smoothed task design matrix D.

Asymptotically, when N_t is sufficiently large, λ is small, and the task waveform is sufficiently slowly varying, Eq. 9 simplifies to an expression independent of D:

$$e_\lambda \approx \left(\frac{g_0}{g_\lambda}\right)^2\left(\frac{tr_m(S_\lambda S_\lambda{}')}{N_t}\right) = \left(\frac{g_0{}^2}{N_t}\right) / \left(\frac{g_\lambda{}^2}{tr_m(S_\lambda S_\lambda{}')}\right) \qquad [11]$$

With $\lambda = 0$ (no smoothing), $tr_m(S_\lambda S_\lambda{}') = N_t$ for all voxels, which naturally leads to defining an approximate DOF expression as:

$$DOF_\lambda \approx tr_m(S_\lambda S_\lambda{}'). \qquad [12]$$

Then Eq. 11 can be interpreted intuitively as the ratio of the squared g-factors (g^2) normalized by their respective DOF. When regularization reduces g-factor faster than the loss of effective DOF, efficiency and statistical power are increased compared to the un-regularized case.

3. Methods

To characterize the proposed method, numerical simulations were performed to validate the analytical g-factor, DOF and efficiency expressions, and to assess signal bias and slice leakage using a realistic signal spectral densities. Experiments were also performed to evaluate reconstruction performance *in vivo*, demonstrate image quality improvements and efficiency gains.

3.1 Numerical Simulations

A single-band reference dataset was acquired on a spherical phantom using a 64-channel head and neck coil to form the basis for numerical simulations, of a MB=8 acquisition with 256 timepoints using 16 compressed virtual coils (Zhang et al., 2013). First, Monte Carlo simulations with Gaussian white additive noise were performed with 1000 different complex noise realizations. To compare the proposed reconstructions against post-hoc smoothing, linear smoothing operators $S_\kappa = (I + \kappa\nabla'\nabla)^{-1}$ were constructed, with κ chosen empirically to match effective DOF with S_λ using Eq. 10.

Next, inter-slice leakage and relative efficiencies were examined by simulating reconstruction of a noise-free dataset with a voxel-wise random signal. A 1/f characteristic of BOLD fMRI data (Zarahn et al., 1997) was used to provide a realistic basis for assessing leakage bias, because residual bias is signal-dependent (Eq. 6) in the proposed reconstruction. To characterize leakage, in this simulation we zeroed out the signal from all slices except slice location 5, such that any signal in the remaining 7 slices constituted leakage. Comparisons against different and multiple CAIPI patterns were explored, with different FOV shifts (, where the sampling pattern is shifted by every phase encoding step by) and different shifts of the sampling pattern over time (, where the sampling pattern is shifted by every successive readout of the same slices) (Figure 1).

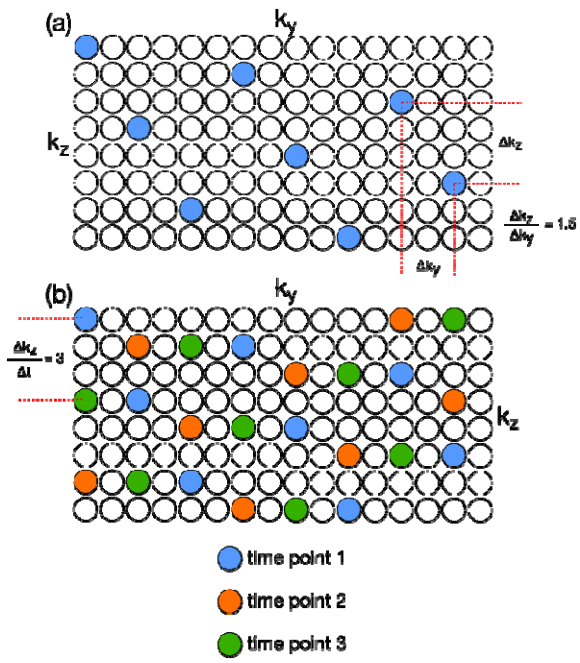

Figure 1 - (a) Example CAIPI sampling pattern for a MB8R2 acquisition. In this example, the $\Delta k_z = 3$, and $\Delta k_y = 2$, leading to a slice-wise CAIPI shift of FOV*3/16. (b) The sampling pattern can be shifted over time, as shown here by a $\Delta k_z/\Delta t = 3$. The time-shifting parameter $\Delta k_z/\Delta t$ does not need to be constant, and can be pseudorandom.

Across the simulations, three different GLM design regressors were initially used to evaluate g-factor, DOF and efficiency: (i) 5-period block design, (ii) fast event-related design, (iii) white noise regressor (see Supporting Figure S1). For compactness, all subsequent efficiencies were calculated with respect to the event-related regressor.

3.2 In Vivo Validation

Three subjects were scanned on a 3 T system (Prisma, Siemens Healthineers) using a 64-channel head and neck coil with informed consent in accordance with local ethics. In two subjects, we used CAIPI k-space sampling, but with a single-band (slice 5) excitation, enabling us to derive a ground truth from the single-slice reconstructions. Both subjects

were scanned with a MB=8, R=1 protocol (MB8R1) with a single-band excitation using $\Delta kz/\Delta ky = 5$ and $\Delta kz/\Delta t = 3$, with TE=38 ms, TR_{vol}=680 ms, 2 mm isotropic resolution with 64 slices. One of the subjects was additionally scanned using a MB=8, R=2 in-plane protocol (MB8R2) using a CAIPI pattern with $\Delta kz/\Delta ky = 5/2$ and $\Delta kz/\Delta t = 3$, with TE=30 ms, TR_{vol}=480 ms, 2 mm isotropic resolution with 64 slices. This same subject was also scanned using these same two protocols, but using full MB=8 excitation.

One additional subject was scanned using the full MB=8 excitation with the MB8R1 protocol in a 30 s off/on block design visual task experiment. All scans were 5 minutes in duration, and sensitivity maps were estimated using the adaptive combine method (Walsh et al., 2000) from a separate single-band reference acquisition, compressed down to 24 virtual channels after whitening with the coil noise covariance.

Empirical temporal SNR (tSNR) efficiency maps were computed from the resting condition data by adjusting the temporal standard deviation with the normalized DOF using the approximate form in Eq. 12:

$$tSNR_{eff} = \frac{mean(|x|)}{std(x)/\sqrt{DOF_\lambda/N_t}} = \frac{mean(|x|)}{std(x)}\sqrt{\frac{DOF_\lambda}{N_t}} \qquad [11]$$

with the mean and standard deviation (std) taken across time. When $DOF_\lambda/N_t = 1$, this is equivalent to conventional tSNR, but when $DOF_\lambda/N_t < 1$, tSNR efficiency decreases to reflect the reduced degrees of freedom per unit time. GLM output t-statistics were estimated from the magnitude transformed visual task data using FSL FEAT with pre-whitening (Woolrich et al., 2001).

3.3 SMS-Reconstruction

Eq. 4 was solved iteratively using a conjugate gradient algorithm implemented in MATLAB, using a tolerance of 10^{-4} and a maximum number of iterations of 200. The g-factor and efficiency expressions were evaluated directly, by partitioning the matrix inversions into smaller independent subproblems by exploiting the independence of each x-location (along the fully-sampled readout direction) and the coherent aliasing patterns when possible. Reconstruction code for the proposed method can be found at https://users.fmrib.ox.ac.uk/~mchiew/research. The *in vivo* data were compared with conventional slice-GRAPPA reconstructions using a MATLAB implementation of the CMRR-SMS (Center for Magnetic Resonance Research, University of Minnesota) reconstruction with the LeakBlock option set.

4. Results

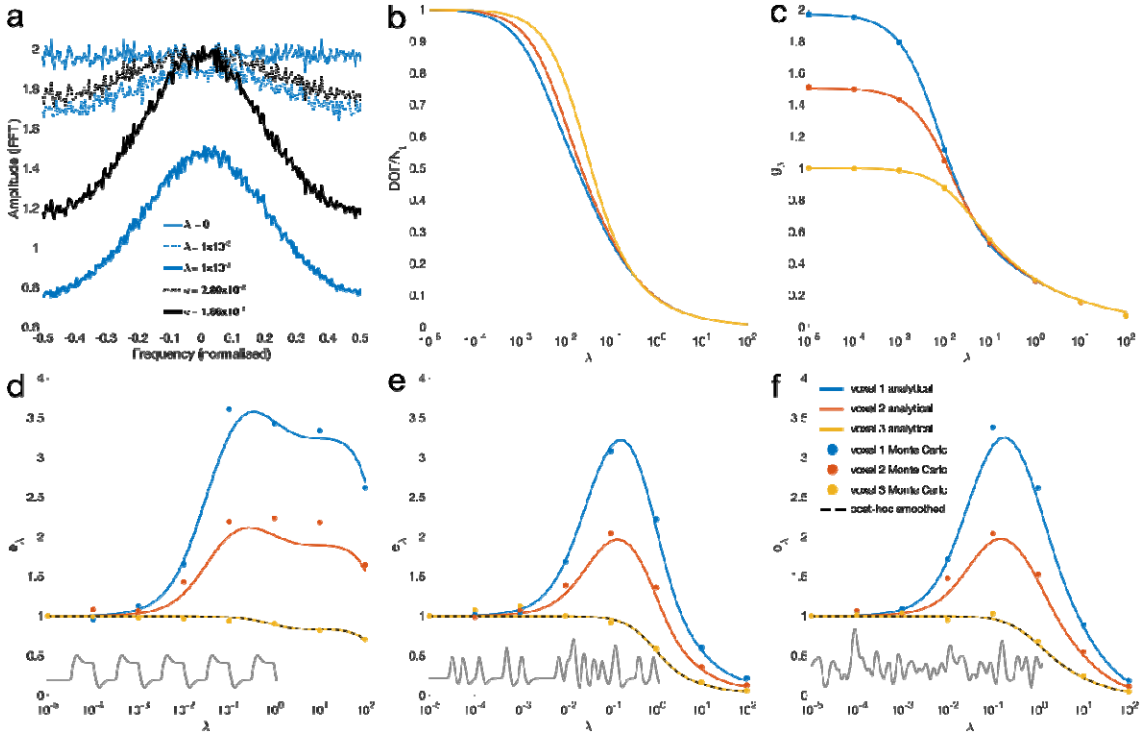

Figure 2 - (a) Average spectra from a representative voxel (voxel 1) showing unregularized (thin blue), (dotted blue), and (thick blue) reconstructions. DOF-matching post-hoc kernel smoothing reconstructions are shown in black dotted and thick lines respectively. (b-f) Analytical plots for 3 voxels showing different behavior (blue, orange, yellow lines) are shown alongside corresponding Monte Carlo estimates (blue, orange, yellow dots), versus (b) Approximate plots. (c) g-factor. (d-f) Exact GLM efficiency combining information from DOF and g-factors, calculated using regressors (shown in the bottom left) corresponding to (d) block design, (e) event-related design and (f) white noise respectively. DOF-matched post-hoc smoothing efficiency is plotted in dashed black, overlapping with voxel 3.

In Fig. 2a, measured noise amplitude spectra are plotted after, and reconstructions, and DOF-matching post-hoc smoothing . As total noise is the sum of squares in either the temporal or frequency domain, it is apparent that the regularized reconstructions result in less noise compared to post-hoc smoothing with the same effective DOF (blue and black lines having similar spectral profiles, but with the blue lines having lower amplitude than the corresponding black lines). As or increases, the effective DOF decreases and the coloring of the noise spectrum is more pronounced as higher frequency content is suppressed. Figs. 2b and 2c plot the variation in approximate DOF (Eq. 12) and g-factor (Eq. 8) respectively against , showing the expected decrease with increasing regularization across the three voxels (selected to reflect a range of behavior). Voxels 1 and 2 show high and moderate g-factor voxels respectively, while voxel 3 does not alias onto any other voxel, with a g-factor of 1.

The relative efficiency metrics (Eq. 9) in Figs. 2d-f, which reflect the ratio of the squared g-factors to the DOF, show that while a net benefit (is observed in the linear smoothing reconstructions for any voxel that has a , there is no gain in efficiency for any voxel that does not alias onto another voxel, where . Post-hoc smoothing (black

dashed line) shows the same efficiency curve as voxel 3, indicating that no efficiency gain is realized. In all cases with an efficiency benefit, increases with , to a maximum in this case near . As gets too large, the loss of DOF in the regression begins to outweigh the reduced g-factors, and statistical power decreases. The efficiency curves for each regressor are unique due to the dependence of DOF on the design matrix. However, they all show very similar characteristics for low values of . They exhibit fairly broad peaks in a logarithmic scale, indicating that near-optimal gains are easily achieved within an order of magnitude of the maxima.

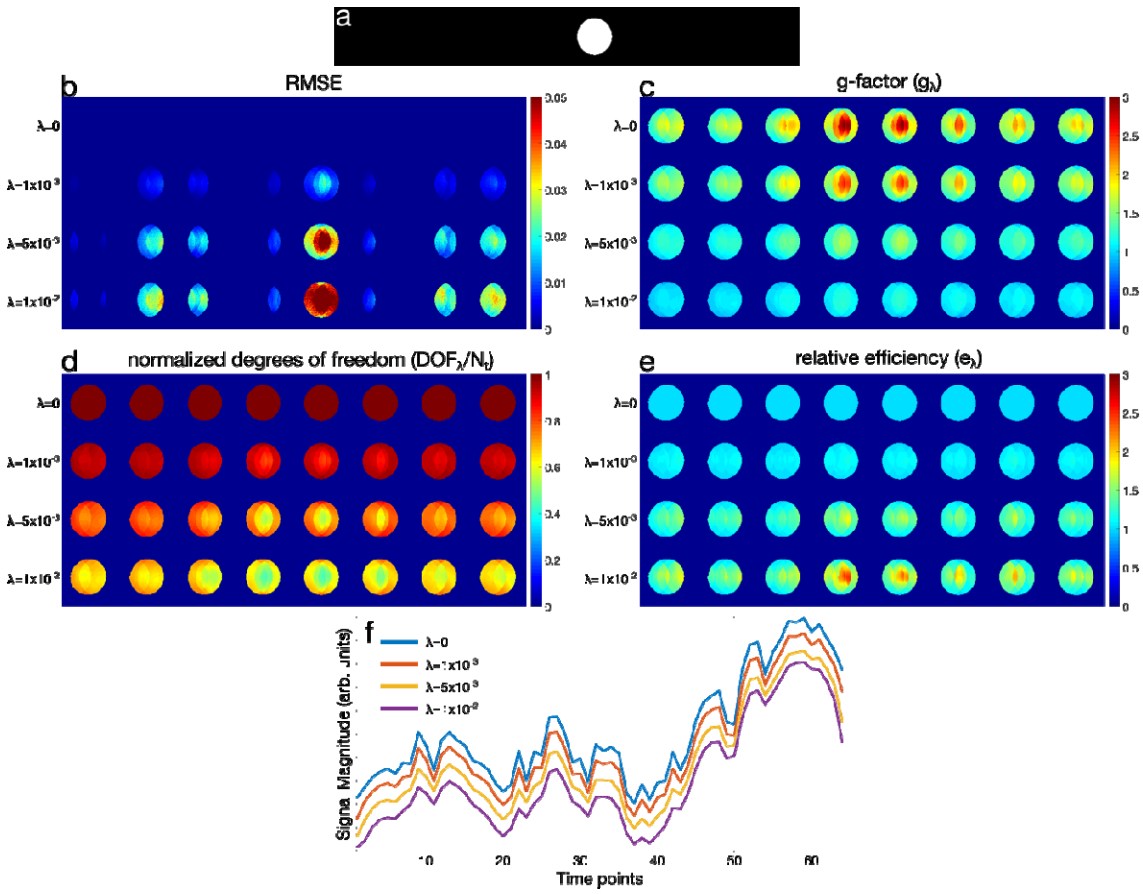

Figure 3 - (a) Single slice phantom simulation (b) normalized root-mean-square error across time, quantifying spatial leakage bias (c) g-factor (d) normalized degrees of freedom ( ) (e) GLM relative efficiency (f) example voxel time-courses

The single-slice digital phantom is shown in Fig. 3a. To assess residual leakage and aliasing, the normalized root mean square error (NRMSE) across time was computed across varying in Fig. 3b, showing an increase in leakage with . The 95th percentiles for the NRMSE values in each case were: , , , and respectively. In Figs. 3c-e, g-factors, , and efficiency are shown. The voxel-wise maps show that the greatest efficiency increases are in regions with the highest unregularized g-factors, which can be seen when comparing row 1 of Fig. 3c with

row 4 of Fig. 3e. Fig. 3f plots a representative voxel time-series showing increasing smoothness in the time-courses as increases.

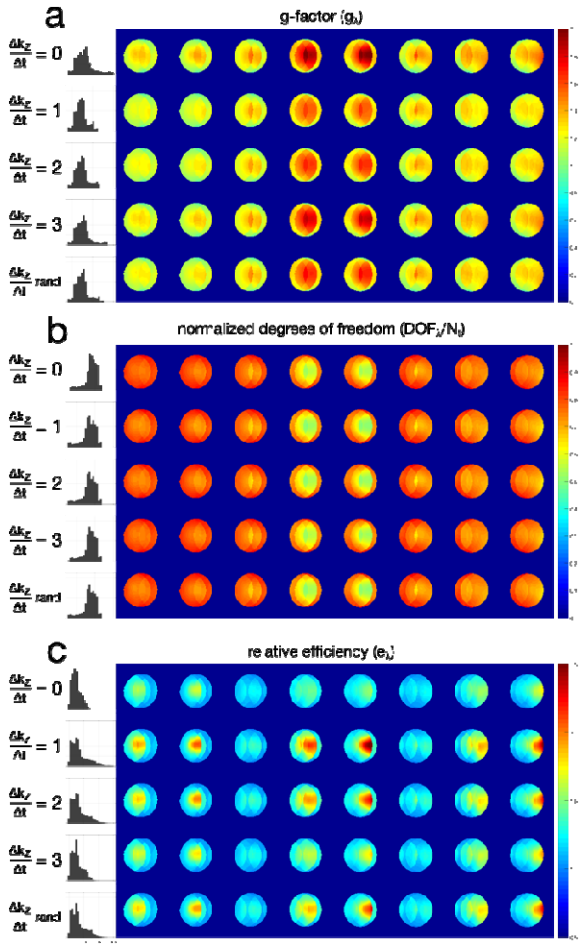

Figure 4 - Digital phantom characteristics with different temporal sampling patterns. (a) g-factor, (b) , (c) GLM relative efficiency. Histograms of the values are shown on the left of each row.

In Fig. 4, the effect of different sampling patterns (at) is shown against fixed, time-independent sampling , and sampling with shifts of 1, 2, or 3 in the direction. Comparisons were also performed against sampling where the shift was pseudorandom at every time-point. A reduction in g-factors (Fig. 4a) with time-varying sampling is shown, without much difference in (Fig. 4b). The net effect on efficiency (Fig. 4c), however, is considerable when compared to time-independent sampling. The top row of Fig. 4c shows that there is still a small efficiency gain with fixed sampling, and even random time-shifting of the sampling pattern produced near optimal efficiencies.

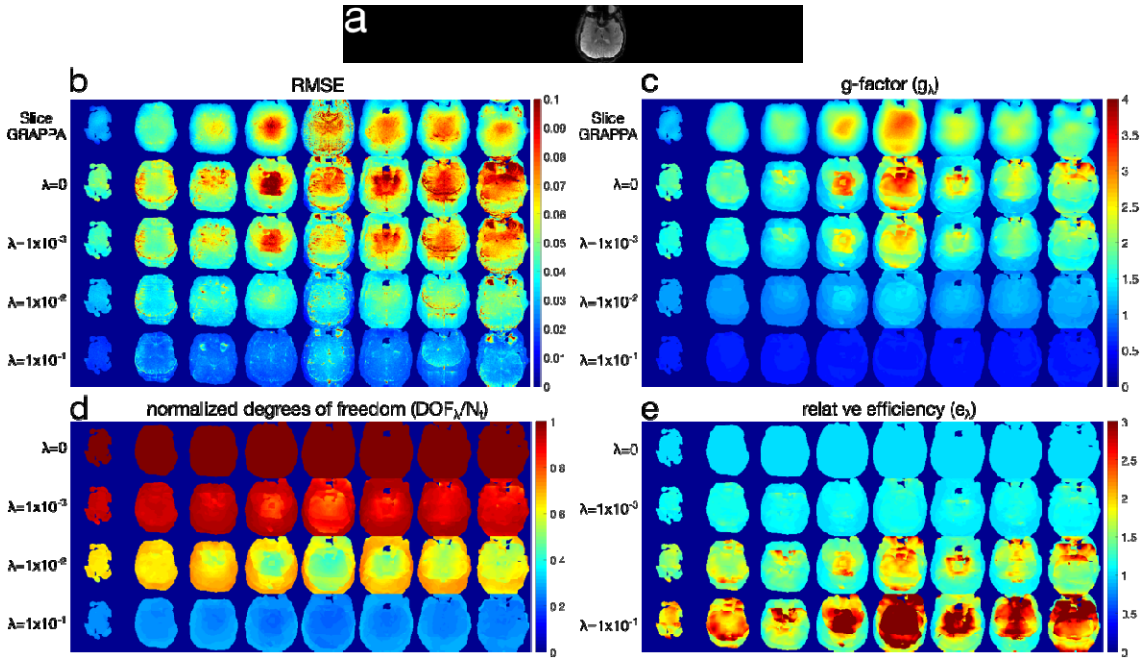

Figure 5 - (a) Single-slice in vivo SMS reconstructions, with (b) normalized root-mean-square error across time, capturing both noise amplification and leakage bias (c) g-factor (d) normalized degrees of freedom ( ) (e) GLM relative efficiency

Single-band excitation *in vivo* data for a single subject using the MB8R1 protocol is shown in Fig. 5, with the voxel-wise RMSE across time (normalized by the RMS signal in the excited slice) in Fig. 5b. Note that the masking of the coil-sensitivities here produces a brain-like outline in the non-excited slices. The errors are notably smoother in the slice GRAPPA reconstruction outside the target slice, with the regularized reconstructions showing lower error at . The errors are visibly noise (g-factor) dominated at low (row i), and bias dominated (leakage or aliasing) at higher (row iv). Figs. 5c-e show g-factors and efficiency respectively, with and for each value reported in Supporting Table S2.

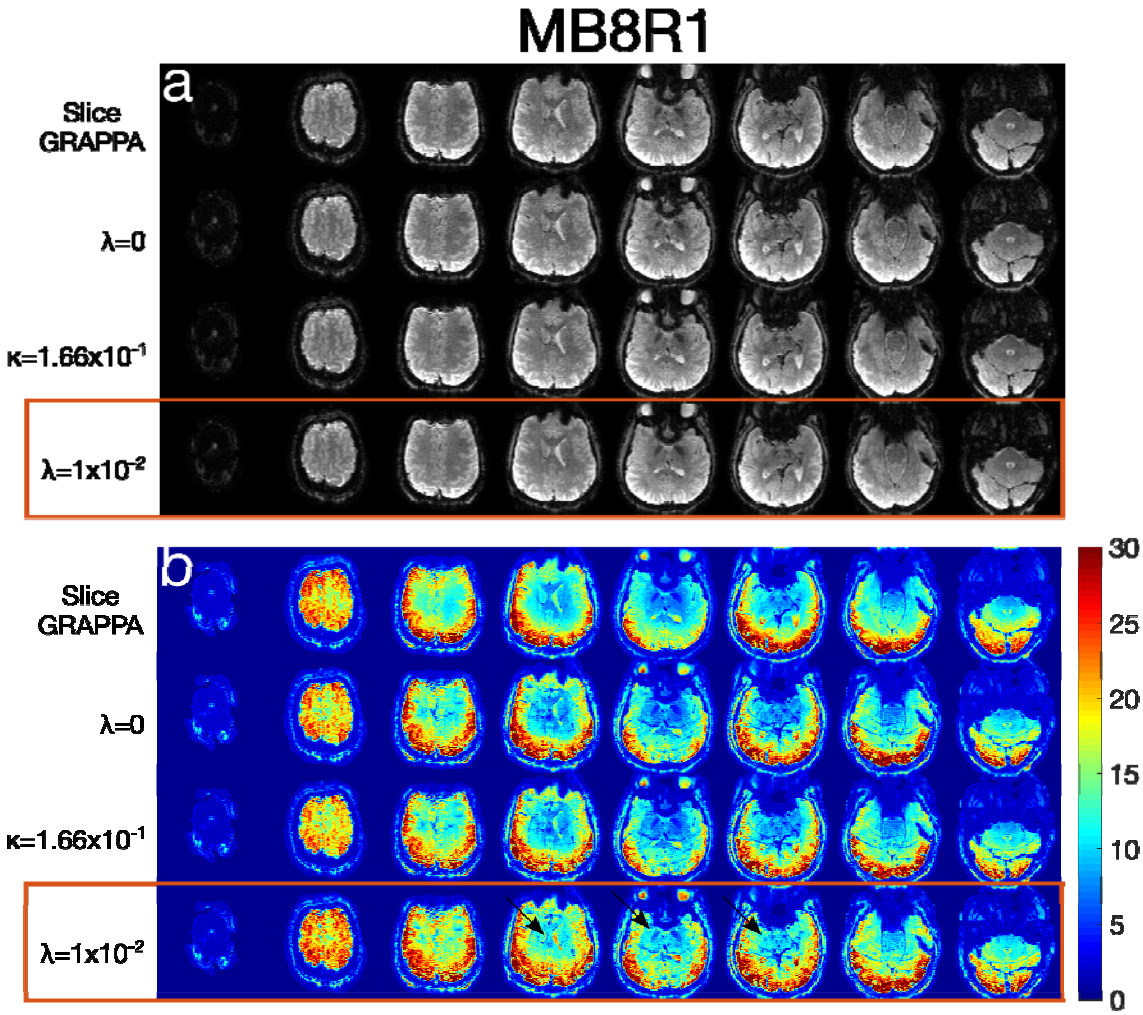

Figure 6 - Representative single time-point reconstructed images (a) and tSNR efficiency (b) for the MB8R1 protocol. The top row shows the slice GRAPPA reconstruction, followed by the ( ) unregularized SENSE reconstruction, and the ( ) post-hoc smoothed data. The orange box highlights the temporally smoothed reconstruction ( ), and the black arrows in (b) denote regions of improved tSNR efficiency.

Figure 6a shows representative images from the fully excited MB8R1 protocol, with visible noise amplification in the slice GRAPPA and unregularized reconstruction (. The tSNR efficiency (Fig. 6b) is visibly improved in central brain areas for the regularized (reconstruction, whereas high SNR cortical regions are less affected. A post-hoc smoothed dataset (, row 3), in contrast, shows no change in tSNR efficiency, as the loss in DOF offsets the reduction in variance due to smoothing. Similar results for the MB8R2 protocol are plotted in Figs. 7a and b, illustrating that the slice GRAPPA, un-regularized and post-hoc smoothing images are unable to unalias the data at this acceleration, even with a large smoothing factor ( ). However, the temporally regularized reconstructions (result in better images and higher tSNR efficiencies, without much visible aliasing, particularly in the case. Additional results assessing improvements in voxel-wise GLM efficiency can be found in Supporting Figure S3.

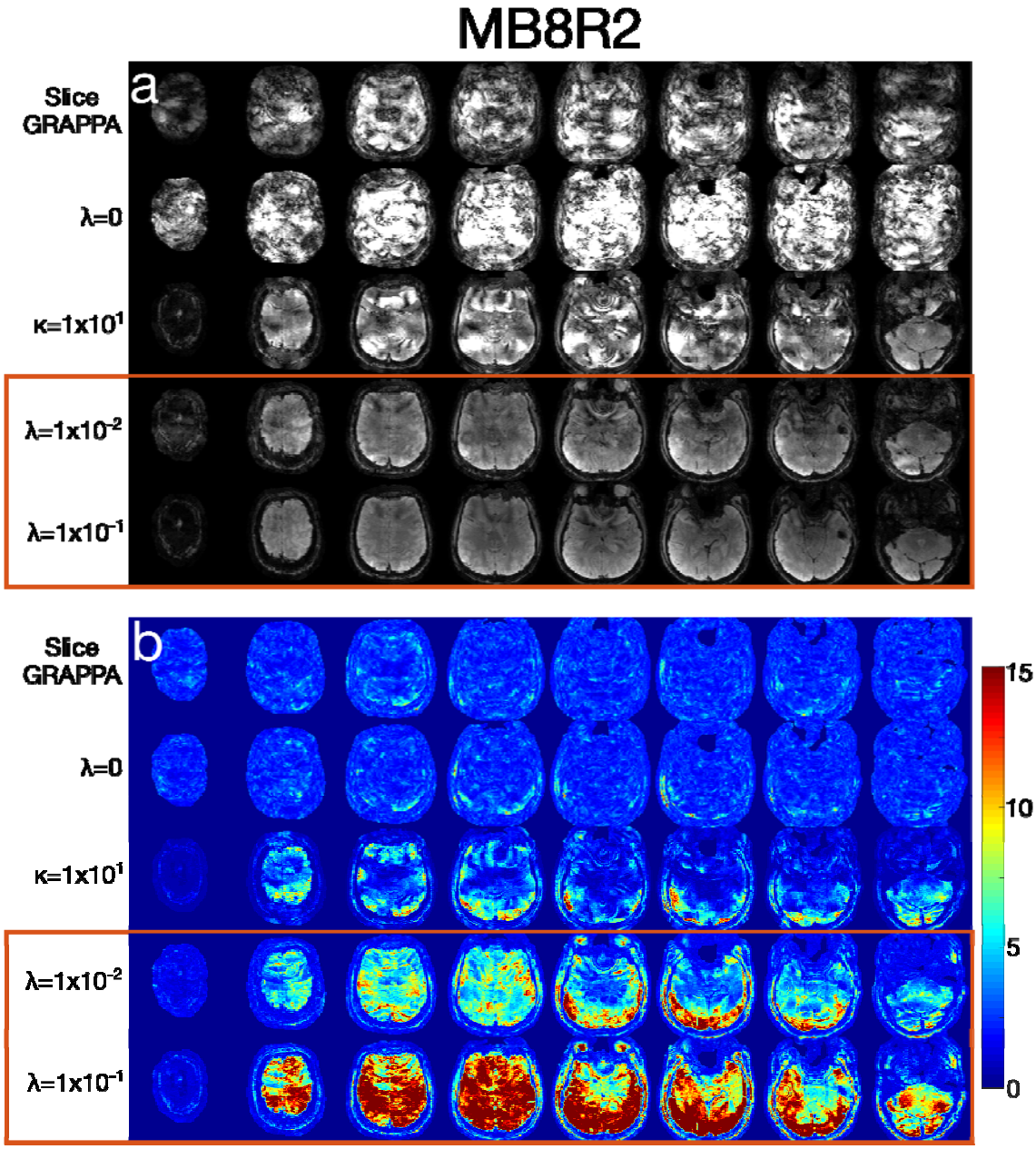

Figure 7 - Representative single time-point reconstructed images (a) and tSNR efficiency (b) for the MB8R2 protocol. The top row shows the slice GRAPPA reconstruction, followed by the ( ) unregularized SENSE reconstruction, and the ( ) post-hoc smoothed data. The orange box highlights the temporally smoothed reconstructions ( ).

The output of a GLM analysis on the visual task block-design MB8R1 dataset is shown in Fig. 8. The underlying images highlight the apparent tSNR difference expected between the slice GRAPPA and reconstructions, particularly noticeable in the sagittal views (Figs. 8b,d). Furthermore, no residual aliasing is apparent in the images or in the z-statistic maps in the proposed regularized reconstruction. While the z-statistic images look qualitatively similar in both cases, due to the peripheral location of the activation, a scatterplot of all the z-statistics (Fig. 8e) shows most of the high z-statistic voxels (e.g. are higher for the reconstruction compared to the slice GRAPPA data.

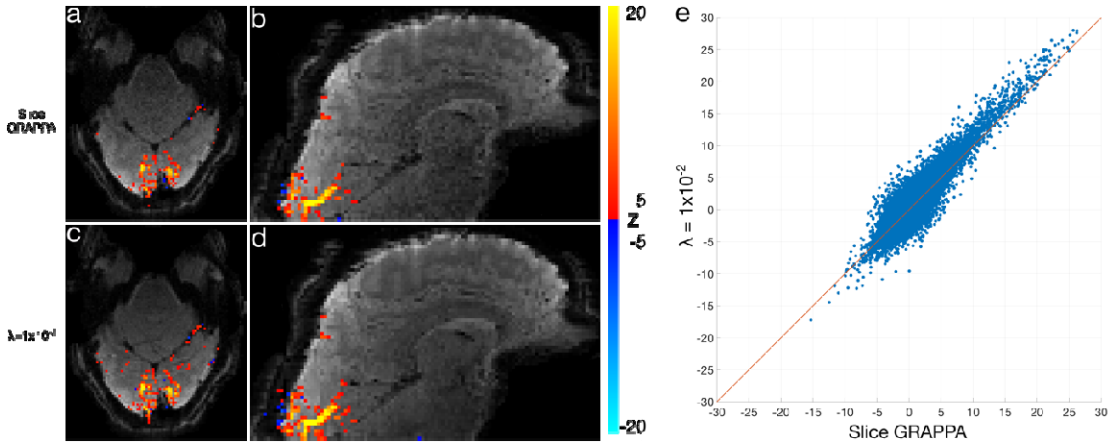

Figure 8 - Visual task fMRI dataset using MB8R1 protocol. (a,b) Axial and sagittal z-statistic maps (overlaid on an example image reconstructed using slice GRAPPA. (c,d) Corresponding slices to (a,b) from regularized SENSE reconstruction. (e) z-statistic scatterplot of all voxels in the reconstruction against the slice GRAPPA, with the line of identity in orange. Points above the line indicate higher z-statistics in the reconstruction compared to slice GRAPPA.

5. Discussion

Reconstruction of SMS fMRI data has predominantly been performed using time independent, volume-by-volume reconstructions based on SENSE or GRAPPA-based equivalents. Here, we propose the use of regularization that modulates temporal smoothness in a spatially adaptive manner, to reduce variance (g-factor) and increase GLM estimation efficiency. Unregularized SENSE reconstructions are unbiased (no leakage) and contrast independent, contingent on the fidelity of the sensitivity estimates. Slice GRAPPA approaches, with limited kernel sizes and dependence on signal contrast changes, trade robustness for residual intra- and inter-slice artefact, effectively allowing for small amounts of bias in the reconstructions to produce better overall images with potentially lower mean squared error. The proposed reconstruction makes a similar trade-off, relying on the low-frequency nature of BOLD signals to ensure that temporal regularization results in comparable or less mean squared error than is produced by conventional slice-GRAPPA unaliasing, while improving statistical efficiency.

A natural question is whether there is any advantage to acquiring data at higher acceleration factors and temporally smoothing in reconstruction compared to acquisition at intrinsically lower temporal resolution. The benefit comes from the spatially adaptive reconstruction, in which smoothing is commensurate to the expected g-factors. In peripheral regions like cortex, where g-factors are low, higher DOF are preserved, whereas greater smoothing and significant DOF reductions only occur in the central brain areas with higher g-factors, to boost statistical power where it is needed most. In contrast, slower acquisitions reduce DOF uniformly across the volume. Although this results in images with

spatially varying DOF, voxel-wise variation in GLM efficiency is already commonplace using conventional parallel imaging due to spatially varying g-factors. Other advantages of acquiring data at higher acceleration factors include reduced intra-volume motion, potentially better contrast, and reduced physiological noise aliasing when slower acquisitions do not sufficiently sample cardiac frequencies.

Spatially varying smoothing is also possible using voxel-wise post-hoc kernel smoothing of varying kernel widths. However, we have shown that post-hoc smoothing with an encoding independent kernel can only reduce the efficiency of the GLM estimator (Liu and Frank, 2004; Smith et al., 2007). The proposed smoothing regularized reconstruction, in contrast, depends on the encoding (i.e. the k-space sampling pattern and coil sensitivities), and reduces noise variance beyond what would be expected from the spectral filtering effect alone. By shifting the noise spectra down, there is a net reduction in variance per degree of freedom, and therefore a benefit to GLM inference. The efficiency measure presented here generalizes the tSNR efficiency commonly used to assess fMRI time-series fidelity, by accounting for the effective degrees of freedom, rather than acquisition time.

As we have shown, the sampling pattern does not need to have a fixed shift across time, although regular sampling does result in the highest efficiency gains. With a fixed increment sampling pattern, where the relative sample locations of temporal neighbors is constant, the g-factors are time-independent. In the case of more general sampling patterns, as with the pseudorandom sampling, the conditioning of the inverse problem associated with any given time-point is dependent on the sampling of its neighbors, resulting in time-dependent g-factors that can be used to assess the impact of noise amplification on individual time-points.

The smoothing parameter λ can be selected using a number of different criteria: an upper limit on the amount of spatial leakage given some signal model, minimizing mean-squared error, maximum efficiency, or minimum retained DOF. The benefit of the latter two choices is that they are signal independent, although typically the maximum efficiency point incurs significant residual aliasing, and smaller values of λ are used to provide efficiency gains without noticeable bias. While the assumption of a low-frequency dominant spectral density was used to justify the use of the temporal regularization by reducing the impact of signal leakage, the efficiency gain only describes the effects on the residual white Gaussian thermal noise, and not coherent signal-like noise components. The presence of other noise sources diminishes the impact of the efficiency gains calculated here, although in g-factor limited regimes the noise would be thermally dominated. Similarly, the magnitude transform constitutes a non-linear operation on the data and alters the noise distribution, but this effect should be negligible when tSNR > 2 (Gudbjartsson and Patz, 1995).

In this work, we focus on statistical efficiency as the primary metric of reconstruction quality, rather than optimizing directly for minimizing noise or maximizing SNR. We explicitly construct the efficiency metric expression by an end-to-end consideration of the fMRI dataset, from noisy multi-coil k-space to the variance of the GLM estimator, which is possible due to the linear reconstruction and analysis framework. While we do not directly optimize for other non-GLM analysis methods, such as independent component or seed-correlation analysis for resting state fMRI, reduced noise variance per DOF should also be beneficial, although this has not yet been evaluated.

6. Conclusion

A linear reconstruction method for SMS-EPI fMRI data has been developed based on temporal smoothing regularization in a spatially adaptive, encoding-dependent way. This reduces noise for improved statistical power in the high g-factor central regions of the brain, while leaving cortical regions less affected, compared to conventional slice-GRAPPA reconstructions.

Appendix A

The recontruction is a linear transform of the measured k-space and a noise term:

$$\hat{x} = (A'A + \lambda\nabla'\nabla)^{-1}A'(k + n) \qquad \text{[A1]}$$

The noise model we assume is zero-mean, Gaussian white noise, with $n = N(0, \sigma)$, and we further assume that the noise has been whitened using the coil noise covariance, so that:

$$E[nn'] = \sigma^2 I \qquad \text{[A2]}$$

The mean or expectation of the estimate (because the noise is zero mean):

$$\bar{x} = E[\hat{x}] = (A'A + \lambda\nabla'\nabla)^{-1}A'k \qquad \text{[A3]}$$

and the mean-subtracted estimate is a function of the noise:

$$(\hat{x} - \bar{x}) = (A'A + \lambda\nabla'\nabla)^{-1}A'n \qquad \text{[A4]}$$

We calculate the g-factor from the voxel-wise variance of the linear estimator:

$$Var(\hat{x}) = E[(\hat{x} - \bar{x})(\hat{x} - \bar{x})'] = E[(A'A + \lambda\nabla'\nabla)^{-1}A'nn'A(A'A + \lambda\nabla'\nabla)^{-1}] \qquad \text{[A5]}$$

Since the noise term is the only stochastic part of this expression:

$$Var(\hat{x}) = (A'A + \lambda\nabla'\nabla)^{-1}A'(\sigma^2 I)A(A'A + \lambda\nabla'\nabla)^{-1} \qquad \text{[A6]}$$

The square root of the entries along the diagonal of $Var(\hat{x})$ reflect the standard deviation of the noise expected in each voxel. The g-factor is calculated as the ratio of this standard deviation with the standard deviation expected from a fully-sampled acquisition. Since the fully-sampled, un-regularized variance in each voxel m is $\sigma^2/(A'A)_{m,t}$, the ratio then becomes:

$$g_\lambda(m,t) = \sqrt{\frac{\sigma^2((A'A+\lambda\nabla'\nabla)^{-1}A'A(A'A+\lambda\nabla'\nabla)^{-1})_{m,t}}{\frac{\sigma^2}{(A'A)_{m,t}}}} \qquad \text{[A7]}$$

$$= \sqrt{((A'A + \lambda\nabla'\nabla)^{-1}A'A(A'A + \lambda\nabla'\nabla)^{-1})_{m,t}(A'A)_{m,t}} \qquad \text{[A8]}$$

$$= \sqrt{(S_\lambda(A'A)^{-1}S_\lambda{}')_{m,t}(A'A)_{m,t}} \qquad \text{[A9]}$$

where $S_\lambda = (A'A + \lambda\nabla'\nabla)^{-1}A'A$, and $X_{m,t}$ denotes the diagonal element of X corresponding to the mth voxel and t^{th} time-point.

Appendix B

In the context of a univariate GLM analysis, a regression coefficient $\hat{\beta}$ can be expressed as a function of S_λ as:

$$\hat{\beta} = \left(\widetilde{D}'\widetilde{D}\right)^{-1}\widetilde{D}'S_\lambda\tilde{x} \qquad \text{[B1]}$$

where $\widetilde{D} = S_\lambda D$ is the smoothed design matrix, assumed to be a single column. More complex contrasts can be accommodated without any loss of generality by a simple transformation (Smith et al., 2007).

From Worsley and Friston (Worsley and Friston, 1995), the variance of the regression coefficient $\hat{\beta}$ is:

$$var(\hat{\beta}) = \epsilon^2\left(\widetilde{D}'\widetilde{D}\right)^{-1}\widetilde{D}'S_\lambda S_\lambda{}'\widetilde{D}\left(\widetilde{D}'\widetilde{D}\right)^{-1} \qquad \text{[B2]}$$

with

$$\epsilon^2 = \frac{g^2\sigma^2}{DOF} \qquad \text{[B3]}$$

and

$$DOF = tr_m\left(\left(I - \widetilde{D}\left(\widetilde{D}'\widetilde{D}\right)^{-1}\widetilde{D}'\right)S_\lambda S_\lambda{}'\right) \qquad \text{[B4]}$$

with $tr_m(\cdot)$ used to indicate that values across time for a given voxel m are summed. In Eq. [B3], we make use of the fact that following reconstruction, the noise variance is amplified by the square of the g-factor. Note that in Worsley et al., the design matrix and smoothing operators are denoted by G and K respectively.

Then benefit of regularization, in the context of the GLM, can be quantified by the relative efficiency of the estimator, where a more efficient estimator has increased sensitivity and statistical power. It is defined by the ratio of the variances of the estimators in the unregularized ($\lambda = 0$) and regularized cases:

$$e_\lambda = \frac{var(\hat{\beta}_0)}{var(\hat{\beta}_\lambda)} = \left(\frac{g_0}{g_\lambda}\right)^2 \frac{tr_m\left(\left(I-\widetilde{D}\left(\widetilde{D}'\widetilde{D}\right)^{-1}\widetilde{D}'\right)S_\lambda S_\lambda{}'\right)}{tr_m\left((I-D(D'D)^{-1}D')\right)} \frac{(D'D)^{-1}}{(\widetilde{D}'\widetilde{D})^{-1}\widetilde{D}'S_\lambda S_\lambda{}'\widetilde{D}(\widetilde{D}'\widetilde{D})^{-1}} \qquad \text{[B5]}$$

which dictates whether the decrease in noise amplification outpaces the loss in effective DOF. When $e_\lambda > 1$, a net benefit in GLM efficiency is observed.

Acknowledgements

The authors would like to thank Steen Moeller for providing the slice GRAPPA reconstruction code. This research was funded by the Royal Academy of Engineering (MC, RF201617\16\23) and the Wellcome Trust (KLM, 202788/Z/16/Z). The Wellcome Centre for Integrative Neuroimaging is supported by core funding from the Wellcome Trust (203139/Z/16/Z).

References

Aggarwal, P., Shrivastava, P., Kabra, T., Gupta, A., 2017. Optshrink LR + S: accelerated fMRI reconstruction using non-convex optimal singular value shrinkage. Brain Inform 4, 65–83. https://doi.org/10.1007/s40708-016-0059-x

Blaimer, M., Breuer, F.A., Seiberlich, N., Mueller, M.F., Heidemann, R.M., Jellus, V., Wiggins, G., Wald, L.L., Griswold, M.A., Jakob, P.M., 2006. Accelerated volumetric MRI with a SENSE/GRAPPA combination. J Magn Reson Imaging 24, 444–450. https://doi.org/10.1002/jmri.20632

Blaimer, M., Choli, M., Jakob, P.M., Griswold, M.A., Breuer, F.A., 2013. Multiband phase-constrained parallel MRI. Magn Reson Med 69, 974–980. https://doi.org/10.1002/mrm.24685

Breuer, F.A., Blaimer, M., Heidemann, R.M., Mueller, M.F., Griswold, M.A., Jakob, P.M., 2005. Controlled aliasing in parallel imaging results in higher acceleration (CAIPIRINHA) for multi-slice imaging. Magn Reson Med 53, 684–691. https://doi.org/10.1002/mrm.20401

Cauley, S.F., Polimeni, J.R., Bhat, H., Wald, L.L., Setsompop, K., 2014. Interslice leakage artifact reduction technique for simultaneous multislice acquisitions. Magn Reson Med 72, 93–102. https://doi.org/10.1002/mrm.24898

Chavarrías, C., Abascal, J.F.P.J., Montesinos, P., Desco, M., 2015. Exploitation of temporal redundancy in compressed sensing reconstruction of fMRI studies with a prior-based algorithm (PICCS). Medical physics 42, 3814–3821. https://doi.org/10.1118/1.4921365

Chiew, M., Graedel, N.N., Mcnab, J.A., Smith, S.M., Miller, K.L., 2016. Accelerating functional MRI using fixed-rank approximations and radial-cartesian sampling. Magn Reson Med 76, 1825–1836. https://doi.org/10.1002/mrm.26079

Chiew, M., Smith, S.M., Koopmans, P.J., Graedel, N.N., Blumensath, T., Miller, K.L., 2015. k-t FASTER: Acceleration of functional MRI data acquisition using low rank constraints. Magn Reson Med 74, 353–364. https://doi.org/10.1002/mrm.25395

Fessler, J.A., Rogers, W.L., 1996. Spatial resolution properties of penalized-likelihood image reconstruction: space-invariant tomographs. Image Processing, IEEE Transactions on 5, 1346–1358. https://doi.org/10.1109/83.535846

Griswold, M.A., Jakob, P.M., Heidemann, R.M., Nittka, M., Jellus, V., Wang, J., Kiefer, B., Haase, A., 2002. Generalized autocalibrating partially parallel acquisitions (GRAPPA). Magn Reson Med 47, 1202–1210. https://doi.org/10.1002/mrm.10171

Gudbjartsson, H., Patz, S., 1995. The rician distribution of noisy mri data. Magnetic Resonance in Medicine 34, 910–914. https://doi.org/10.1002/mrm.1910340618

Hoge, W.S., Setsompop, K., Polimeni, J.R., 2018. Dual-polarity slice-GRAPPA for concurrent ghost correction and slice separation in simultaneous multi-slice EPI. Magnetic Resonance in Medicine 80, 1364–1375. https://doi.org/10.1002/mrm.27113

Jung, H., Ye, J.C., Kim, E.Y., 2007. Improved k-t BLAST and k-t SENSE using FOCUSS. Phys. Med. Biol 52, 3201–3226. https://doi.org/10.1088/0031-9155/52/11/018

Kim, T.H., Haldar, J.P., 2015. SMS-LORAKS: Calibrationless simultaneous multislice MRI using low-rank matrix modeling. Presented at the Proceedings - International Symposium on Biomedical Imaging, pp. 323–326. https://doi.org/10.1109/ISBI.2015.7163878

Koopmans, P.J., 2017. Two-dimensional-NGC-SENSE-GRAPPA for fast, ghosting-robust reconstruction of in-plane and slice-accelerated blipped-CAIPI echo planar imaging. Magnetic Resonance in Medicine 77, 998–1009. https://doi.org/10.1002/mrm.26179

Li, X., Ma, X., Li, L., Zhang, Z., Zhang, X., Tong, Y., Wang, L., Sen Song, Guo, H., 2018. Dual-TRACER: High resolution fMRI with constrained evolution reconstruction. Neuroimage 164, 172–182. https://doi.org/10.1016/j.neuroimage.2017.02.087

Liu, T.T., Frank, L.R., 2004. Efficiency, power, and entropy in event-related FMRI with multiple trial types: Part I: theory. NeuroImage 21, 387–400. https://doi.org/10.1016/j.neuroimage.2003.09.030

Moeller, S., Vu, A.T., Auerbach, E., Ugurbil, K., Yacoub, E., 2014. RO extended FOV SENSE/GRAPPA for multiband imaging with FOV shift, in: Proceedings of the 22nd Annual Meeting of ISMRM, 4396. Presented at the Proceedings of the 22nd Annual Meeting of ISMRM, p. 1.

Moeller, S., Yacoub, E., Olman, C.A., Auerbach, E., Strupp, J., Harel, N., Ugurbil, K., 2010. Multiband multislice GE-EPI at 7 tesla, with 16-fold acceleration using partial parallel imaging with application to high spatial and temporal whole-brain fMRI. Magn Reson Med 63, 1144–1153. https://doi.org/10.1002/mrm.22361

Park, S., Park, J., 2017. SMS-HSL: Simultaneous multislice aliasing separation exploiting hankel subspace learning. Magn Reson Med 78, 1392–1404. https://doi.org/10.1002/mrm.26527

Petrov, A.Y., Herbst, M., Andrew Stenger, V., 2017. Improving temporal resolution in fMRI using a 3D spiral acquisition and low rank plus sparse (L+S) reconstruction. Neuroimage 157, 660–674. https://doi.org/10.1016/j.neuroimage.2017.06.004

Pruessmann, K.P., Weiger, M., Scheidegger, M.B., Boesiger, P., 1999. SENSE: sensitivity encoding for fast MRI. Magn Reson Med 42, 952–962.

Ramb, R., Binter, C., Schultz, G., Assländer, J., Breuer, F., Zaitsev, M., Kozerke, S., Jung, B., 2015. A g-factor metric for k-t-GRAPPA- and PEAK-GRAPPA-based parallel imaging. Magn Reson Med 74, 125–135. https://doi.org/10.1002/mrm.25386

Setsompop, K., Gagoski, B.A., Polimeni, J.R., Witzel, T., Wedeen, V.J., Wald, L.L., 2012. Blipped-controlled aliasing in parallel imaging for simultaneous multislice echo planar imaging with reduced g-factor penalty. Magn Reson Med 67, 1210–1224. https://doi.org/10.1002/mrm.23097

Singh, V., Tewfik, A.H., Ress, D.B., 2015. Under-sampled functional MRI using low-rank plus sparse matrix decomposition, in: ICASSP 2015 - 2015 IEEE International Conference on Acoustics, Speech and Signal Processing (ICASSP). Presented at the ICASSP 2015 - 2015 IEEE International Conference on Acoustics, Speech and Signal Processing (ICASSP), IEEE, pp. 897–901. https://doi.org/10.1109/ICASSP.2015.7178099

Smith, S., Jenkinson, M., Beckmann, C., Miller, K.L., Woolrich, M.W., 2007. Meaningful design and contrast estimability in FMRI. Neuroimage 34, 127–136. https://doi.org/10.1016/j.neuroimage.2006.09.019

Walsh, D.O., Gmitro, A.F., Marcellin, M.W., 2000. Adaptive reconstruction of phased array MR imagery. Magn Reson Med 43, 682–690.

Weizman, L., Miller, K.L., Eldar, Y.C., Chiew, M., 2017. PEAR: PEriodic And fixed Rank separation for fast fMRI. Medical physics 44, 6166–6182. https://doi.org/10.1002/mp.12599

Woolrich, M.W., Ripley, B.D., Brady, M., Smith, S.M., 2001. Temporal autocorrelation in univariate linear modeling of FMRI data. Neuroimage 14, 1370–1386. https://doi.org/10.1006/nimg.2001.0931

Worsley, K.J., Friston, K.J., 1995. Analysis of fMRI time-series revisited--again. Neuroimage 2, 173–181. https://doi.org/10.1006/nimg.1995.1023

Zahneisen, B., Ernst, T., Poser, B.A., 2014. SENSE and simultaneous multislice imaging. Magn Reson Med 74, 1356–1362. https://doi.org/10.1002/mrm.25519

Zarahn, E., Aguirre, G.K., D'Esposito, M., 1997. Empirical analyses of BOLD fMRI statistics. I. Spatially unsmoothed data collected under null-hypothesis conditions. Neuroimage 5, 179–197.

Zhang, T., Pauly, J.M., Vasanawala, S.S., Lustig, M., 2013. Coil compression for accelerated imaging with Cartesian sampling. Magn Reson Med 69, 571–582. https://doi.org/10.1002/mrm.24267

Zhu, K., Kerr, A., Pauly, J.M., 2012. Autocalibrating CAIPIRINHA: Reformulat- ing CAIPIRINHA as a 3d problem, in: Proceedings of the 20th Annual Meeting of ISMRM. Presented at the Proceedings of the 20th Annual Meeting of ISMRM.

Zong, X., Lee, J., John Poplawsky, A., Kim, S.-G., Ye, J.C., 2014. Compressed sensing fMRI using gradient-recalled echo and EPI sequences. Neuroimage 92C, 312–321. https://doi.org/10.1016/j.neuroimage.2014.01.045